

Greenspan acoustic viscometer: Numerical calculations of fields and duct-end effects

James B. Mehl

National Institute of Standards and Technology, Physical and Chemical Properties Division, Gaithersburg, Maryland 20899 and Department of Physics and Astronomy, University of Delaware, Newark, Delaware 19711-2570

(Received 20 October 1998; accepted for publication 14 April 1999)

Inertial and resistive end corrections for the Greenspan acoustic viscometer were computed using a boundary-integral-equation technique for determination of the acoustic field. Viscous effects were estimated using a boundary-layer approximation. The results apply to a circular duct coupling two concentric chambers and to ducts terminated by infinite plane baffles. The effects of rounding the sharp edge at the duct end were investigated and found to be described by simple scaling relations.

© 1999 Acoustical Society of America. [S0001-4966(99)05507-1]

PACS numbers: 43.20.Mv, 43.20.+g [DEC]

INTRODUCTION

The Greenspan acoustic viscometer (Fig. 1) consists of a cylindrical duct coupling two chambers whose volumes are large compared with the volume of the duct. Gillis *et al.*^{1,2} have shown that the Greenspan viscometer is an accurate and convenient device for measuring the viscosity of gases. A full theory of the viscometer requires modeling the inertial and viscous effects of the convergent/divergent flow at the duct ends. These effects are investigated numerically in this paper. The present results are required if the uncertainty of viscosity measurements is to be reduced from approximately 1% to the order of 0.1%.

The theory of the Greenspan viscometer is based on the linear equations introduced by Kirchhoff to describe the coupled temperature, pressure, and velocity fields in gases.³ In particular, the exact solutions of Kirchhoff are used to calculate the flow impedance of the viscometer duct. For infinitely long ducts and the range of parameters in typical applications, the calculations of the duct impedance can be regarded as exact. End corrections are, however, important for the ducts of convenient experimental designs.

In this work the acoustic field Φ and eigenvalue k are calculated for model shapes in the approximation of rigid boundaries and negligible dissipation. From these solutions, it is possible to determine the inertial end correction without further approximation, and to determine the first-order coefficient of viscous end effects.

A boundary-integral-equation (BIE) formalism was used in the calculations. For axisymmetric shapes like the Greenspan viscometer, the boundary value problem for the acoustic field can be expressed as a one-dimensional integral equation whose solution yields both the eigenvalue k and the eigenfunction, or velocity potential, Φ . This integral equation has been solved for Greenspan viscometers with a wide variety of dimensions. Analysis of the numerical results yielded values of the inertial and resistive end corrections. Among the advantages of the BIE technique is the exact representation of surfaces generated by rotating curves of arbitrary shape. Thus it has been possible to alter the resonator cross-section by replacing sharp corners with chamfered

corners, and to evaluate the effects of chamfering on the inertial and resistive end corrections. Experimental determinations² of the inertial and resistive end effects are in good agreement with the calculations reported here.

The paper is organized as follows. The next section is a review of the acoustic model of the Greenspan viscometer, with emphasis on defining the parameters which need to be evaluated numerically. Some supporting material is in Appendix A. Duct-end effects are discussed in Sec II. Section III is a summary of the numerical approach, with further detail in Appendix B. The remainder of the paper is a presentation and discussion of the numerical results.

I. GREENSPAN VISCOMETERS

Martin Greenspan suggested the use of a double-Helmholtz resonator for measuring the viscosity of gases in 1953.⁴ Recent experimental work^{1,2} demonstrated that such resonators, now called Greenspan viscometers, are capable of measuring the viscosity of gases with an uncertainty less than 1%. Figure 1 shows the viscometer shape and defines some dimensions used throughout this paper. A cylindrical coordinate system concentric with the duct and chambers, with the origin at the center of the resonator, will also be assumed, unless noted otherwise.

The Greenspan viscometer has a low frequency mode in which the gas in the duct oscillates between the two chambers. For this mode, the contours in Fig. 2 show that the acoustic velocity within the duct is nearly constant. A zero-order approximation to the (circular) oscillation frequency can be obtained by assuming that gas in the duct has a constant velocity, and that the main effect of the chambers is a pure compliance. This leads to

$$\omega_0^2 = \frac{2c^2 A_d}{L_d V_c}, \quad (1)$$

where c is the speed of sound, A_d is the cross-sectional area of the duct, L_d is the length of the duct, and V_c is the volume of a single chamber. For practical viscometers, the product of the corresponding propagation parameter $k_0 = \omega_0/c$ and a typical resonator dimension is small compared with unity.

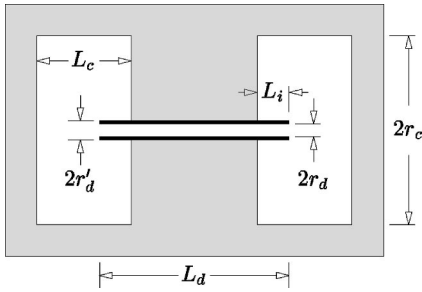


FIG. 1. Cross-section of Greenspan viscometer. The shaded portions are metal; the gas under test fills the open areas of the resonator. The transducers and fill duct are omitted.

Practical acoustic viscometers must be described by an acoustic model which includes viscous and thermal dissipation. The model is defined most succinctly by an equivalent circuit of acoustic elements.¹ The duct element is a T -equivalent circuit which represents the Kirchhoff equations.³ The duct ends and the chambers are represented by series combinations of orifice impedances Z_{end} and chamber impedances Z_V . Each of these lumped-circuit components is defined as the ratio of an acoustic pressure difference divided by a volume velocity. The chamber impedances can be modeled with accurate analytic approximations which include the effects of the thermal boundary layers at the chamber walls. The acoustic velocity field in the chambers is negligibly small except for the region within a few duct radii of the duct end. The inertial and dissipative effects of the velocity field within the chamber are thus localized and are most conveniently included in the orifice impedance.

The Kirchhoff equations provide an essentially exact description of the coupled pressure, temperature, and vorticity fields in ducts of infinite length. At the Helmholtz resonance of the viscometer, the flow in the duct is nearly uniform with a pressure node at $z=0$. This point is also a node for the acoustic temperature. The full theory shows that temperature oscillations in the duct are so weak that dissipation in the duct is almost entirely due to viscous effects. (The full model accounts for the small thermal losses in the chambers.¹)

Near the ends of the duct the Kirchhoff equations fail to represent the field accurately. The full solution in the duct could in principle be represented as the sum of the contributions from a single propagating mode and an infinite number of evanescent modes. The latter decay within a few duct radii

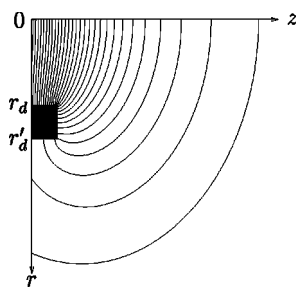


FIG. 2. The acoustic field near a duct end, for radial coordinate $r \geq 0$ and axial coordinate z along the axis of symmetry of the viscometer. The dark rectangle represents a half-cross-section of the end of a duct wall between radii r_d and r'_d . The field is shown as contours of uniformly spaced velocity potential (or pressure), as calculated in this work.

of the ends. The viscous and inertial effects of the evanescent waves, and the viscous and inertial effects of localized fields in the chambers near the orifices, are included in the orifice impedance. An approximate theory of the end effects is developed in the next section.

II. DUCT-END EFFECTS

The acoustic fields near acoustic orifices in thin plates and at the ends of ducts have been widely investigated.⁵⁻²⁵ The inertial effects are commonly expressed in terms of a lumped impedance $i\omega\rho\delta_l/A_d$. Here ρ is the gas density, $i\omega\rho/A_d$ is the inertance per unit length for nondissipative acoustic flow in a duct, and δ_l is the inertial end correction. Rayleigh⁵ gives the exact value $\delta_l = \pi r_d/4$ for an orifice in an infinitesimally thin plate, and obtained an approximate value $\delta_l \approx 0.82r_d$ for a duct end with an infinite plane baffle. The latter estimate was improved by Daniell,⁶ and recently recalculated by Norris and Sheng,²⁴ who obtained $0.82159r_d$. Rayleigh's expression for the exact flow velocity in the infinitesimally thin orifice $u_z \propto 1/\sqrt{1-r^2/r_d^2}$ has a singularity of order $s^{-1/2}$ at the orifice edge, where s is the distance from the edge. The tangential velocity on the plate has a similar singularity.¹⁰ The weaker singular behavior near the corner of an baffled end, $s^{-1/3}$, was built into the trial solutions used by Daniell. Unbaffled duct ends were investigated by Levine and Schwinger.⁹ In the limit of an infinitesimally thin duct wall, the velocity near the end of the duct has a singularity of order $s^{-1/2}$, and the inertial end correction is approximately $0.61r_d$. As the thickness of the duct wall is increased from very small to large values, the inertial end correction varies uniformly between the limits for thin ducts and infinitely baffled ducts.^{20,25}

Viscous forces associated with the divergences in the tangential flow near a duct end are the sources of additional contributions to the orifice impedance, which can be estimated (in the linear regime) using ideas that were apparently first applied to orifices by Nielsen.^{10,16} The flow is represented by a superposition of acoustic and vorticity waves which together satisfy a nonslip boundary condition on solid boundaries. The vorticity waves are confined to a layer near the solid boundaries of approximate thickness $\delta_v = \sqrt{2\eta/\rho\omega}$, where η is the viscosity. When the viscous penetration length δ_v is small compared with other dimensions, and the surface curvature is large compared with δ_v , the transverse flow velocity near a boundary is approximately

$$u_t(\xi) \approx u_{a,t} [1 - e^{-(1+i)\xi/\delta_v}], \quad (2)$$

where ξ is the distance from the duct wall, and $u_{a,t}$ is the transverse acoustic velocity near the wall. The corresponding force per unit area of boundary surface is

$$\eta \left. \frac{\partial u_t}{\partial \xi} \right|_{\xi=0} = \frac{\eta}{\delta_v} (1+i) u_{a,t} = \frac{1}{2} \rho \omega \delta_v (1+i) u_{a,t}. \quad (3)$$

Nielsen estimated the orifice resistance by integrating the corresponding rate of dissipation per unit area, $\frac{1}{4}\rho\omega\delta_v u_{a,t}^2$. In his application to an orifice in a thin plate, the divergent integral had to be cut off at distance of order δ_v from the orifice edge. For duct ends, the weaker divergence in the

tangential flow velocity leads to a convergent integral, similar to the treatment of step-discontinuities in an infinite plane duct by Morse and Ingard.²⁶

Panton and Miller²² correlated the work of Thurston,¹¹ Ingard,¹⁶ Thurston *et al.*,¹⁷ and Ingard and Ising¹⁹ on the impedance of orifices in thin plates. They found that the orifice inertance was constant below a mean orifice flow velocity of about $0.3 \delta_v \omega$, and that the orifice resistance was constant below a mean orifice flow velocity of about $2 \delta_v \omega$. These results support the existence of a low-velocity linear regime, where the Greenspan viscometer is intended to operate. The nonlinearity thresholds for thin plates and baffled duct ends may differ considerably, however, because the singular behavior of the tangential velocity in the limit of zero viscosity is different for the two cases.

The combined inertial and viscous contributions to the orifice impedance can be conveniently expressed

$$\mathbf{Z}_{\text{end}} = \frac{\rho \omega}{A_d} [i \delta_I + (i+1) \delta_R], \quad (4)$$

where the two components associated with the viscous boundary layer are represented by the orifice resistance parameter δ_R . This parameter can be determined by calculating the additional dissipation near the duct end.²⁶

The total, time-averaged, rate of energy loss due to the viscous boundary layer in an axisymmetric resonator is

$$P = \frac{\pi}{2} \rho \omega \delta_v \int u_{a,t}^2 r ds, \quad (5)$$

where ds is the element of arc length in the longitudinal cross-section of the viscometer. A portion P_0 of this loss will be included in the Kirchhoff equations representing the duct. The acoustic velocity in the duct, in the limit of small δ_v/r_d , is $u_z = u_{z0} \cos kz$, where $k = \omega/c$, so that

$$P_0 = \frac{\pi}{2} \rho \omega \delta_v r_d u_{z0}^2 \int_0^{L_d/2} \cos^2 kz dz. \quad (6)$$

The total power loss

$$P = P_0 + \frac{1}{2} (\rho \omega \delta_R / A_d) U^2 \quad (7)$$

exceeds P_0 because of the localized additional losses near the duct end. Here $U = A_d u_{z0} \cos(kL_d/2)$ is the volume flow out of the duct. Equation (7) can be used to determine δ_R once the total power loss has been determined numerically.

The inertial length δ_I can be obtained most conveniently and with high accuracy by using the resonance condition

$$k \tan(kL_d/2) + k^2 \delta_I - A_d / V_c = 0, \quad (8)$$

derived from the equivalent-circuit model of the viscometer,¹ together with numerically determined values of the resonance parameter k . An alternative procedure, described later, is more directly related to the definition of inertance, but is less convenient because it requires calculation of the flow in the orifice at the duct end. The two methods yield equivalent results.

III. NUMERICAL APPROACH

In the limit of small dissipation, the acoustic pressure within the resonator is proportional to the velocity potential Φ , a solution of the boundary value problem

$$\begin{aligned} (\nabla^2 + k^2) \Phi(\mathbf{r}) &= 0, \quad \mathbf{r} \in C, \\ \frac{\partial \Phi}{\partial n} &= 0, \quad \mathbf{r} \in S, \end{aligned} \quad (9)$$

i.e., the Helmholtz equation in the resonator C subject to a Neumann boundary condition on the resonator surface S . An equivalent form of the same boundary value problem is the integral equation

$$\Phi(\mathbf{r}') \Omega(\mathbf{r}') = - \int_S \Phi(\mathbf{r}) \mathbf{n} \cdot \nabla G(\mathbf{r}', \mathbf{r}) dS, \quad (10)$$

where \mathbf{r} and \mathbf{r}' are both on S , $\Omega(\mathbf{r}')$ is the internal solid angle subtended by S at \mathbf{r}' , and the fundamental solution, or Green's function, is

$$G(\mathbf{r}', \mathbf{r}) = \frac{e^{ikR}}{R}, \quad R = |\mathbf{r} - \mathbf{r}'|. \quad (11)$$

Solutions of this integral equation yield both the eigenfrequency $\omega = ck$ and the velocity potential Φ on the surface of the resonator. The numerical procedure described below enables the determination of smooth approximate values of the tangential velocity $u_{a,t} = \Phi'$ on the resonator boundary, as required for accurate calculations of δ_R .

The cross-sectional area of a Greenspan viscometer, which is both axisymmetric and has mirror symmetry with respect to the $z=0$, plane can be represented by parametric equations $r(t)$ and $z(t)$, both symmetric in t , with the mid-plane at $t=0$. The velocity potential on the surface can be written as a function of the parameter t . In Appendix B it is shown that $\Phi(t)$ is the solution of a one-dimensional integral equation

$$-\Omega(t') \Phi(t') = \int g_n(t', t) \Phi(t) h(t) r(t) dt, \quad (12)$$

where ds , the element of arc length in the cross-section, is equal to $h(t) dt$, and $g_n(t', t)$, is a kernel with a logarithmic singularity at $t=t'$.

An approximate solution of the integral equation (12) can be formulated as a series of Hermite cubic polynomials, each defined on a portion of the boundary. The solutions of interest have odd symmetry $\Phi(t) = -\Phi(-t)$. It suffices to define the geometry for $z \geq 0$ and to use this symmetry in formulating a solution. It is convenient to divide the resonator cross-section, or generator, for $z \geq 0$, into N elements, with the j th element corresponding to $j-1 \leq t \leq j$. The elements could be chosen to have arbitrary shapes. However, shapes with sharp and rounded corners can be represented with only two types of elements: straight lines and circular arcs. The resonator shape is treated exactly within these constraints.

The velocity potential $\Phi(t)$ is approximated as a series of cubic Hermite polynomials so that, by construction, both $\Phi(t)$ and the tangential derivative $\Phi' = d\Phi/ds$ are continu-

ous at the nodes dividing the elements. (The latter condition cannot be applied at reentrant corners, as explained below.) The coefficients in the polynomial representation are the eigenfunction Φ_j and its tangential derivative Φ'_j at nodes $j=0,1,\dots,N$. There are thus $2(N+1)$ unknown coefficients in the representation of the eigenfunction and its derivatives. By requiring that the approximate solution satisfy the integral equation (12) at each of the nodes, $N+1$ linear equations are obtained. Additional linear equations can be obtained by requiring that the second derivatives Φ'' be continuous at most of the internal nodes. This condition must be modified at corners, as described below. Two additional conditions are $\Phi(0)=0$ (at the plane of mirror symmetry) and $\Phi'=0$ for nodes on the axis (unless there is a cusp in the chamber cross-section). With appropriate conditions at each internal node, a total of $N+1$ additional linear equations is obtained. The solution to this set has the form

$$\Phi'_j = \sum_{l=0}^N D_{jl} \Phi_l. \quad (13)$$

The tangential derivatives can now be eliminated from the $N+1$ equations which approximate Eq. (12); this set can now be expressed

$$\sum_{j=0}^N A_{ij}(k) \Phi_j = 0, \quad (14)$$

where the matrix elements $A_{ij}(k)$ are obtained by numerical integration over the elements of appropriate products of the basis functions and the kernel of the integral equation, and subsequent elimination the Φ'_j terms through Eq. (13).

Approximate values of the eigenvalue k are obtained by requiring the determinant of matrix $A_{ij}(k)$ to vanish. Once k is determined, Φ_j can be determined from Eq. (14), and Φ'_j from Eq. (13). Smoother value of Φ_j and Φ'_j can be obtained by solving Eq. (14) by inverse iteration.²⁷

A. Corners

Near corners the eigenfunctions will have a two-dimensional character whose limiting behavior is restricted by the boundary conditions. Consider a (temporary) cylindrical coordinate system with polar coordinates (ζ, ρ, ϕ) . Assume that the ζ axis corresponds to a corner and that the boundaries are at $\phi=0$ and ϕ_c , i.e., ϕ_c is the interior angle at the corner. Solutions of the Helmholtz equation expanded about the corner have the form

$$\Phi = \sum_l [a_l \cos(\mu_l \phi) + b_l \sin(\mu_l \phi)] J_{\mu_l}(k\rho). \quad (15)$$

The Neumann boundary condition, $\partial\Phi/\partial\phi=0$ at $\phi=0$ and $\phi=\phi_c$, requires that all $b_l=0$ and that $\mu_l\phi_c$ be a multiple of π . Accordingly, the lowest nonzero Bessel-function index is $\mu_1 = \pi/\phi_c$. For a $\frac{1}{2}\pi$ internal corner this is $\mu_1 = 2$; for a $\frac{3}{2}\pi$ reentrant corner it is $\mu_1 = \frac{2}{3}$. The leading term in the expansion of the Bessel function is $(k\rho)^{\mu_1}$. Accordingly, at $\frac{1}{2}\pi$ internal corners the eigenfunction Φ will have a vanishing tangential derivative as the corner is approached. This is

the supplementary condition used instead of continuity of Φ'' at corner nodes with interior angle $\frac{1}{2}\pi$.

For a $\frac{3}{2}\pi$ reentrant corner at node l_c the eigenfunction will have a limiting behavior of the form, with $s-s_c$ the arc length from the corner and C a constant,

$$\Phi = \Phi_{l_c} \pm C |s-s_c|^{2/3}, \quad (16)$$

which has a singular tangential derivative. An improved approximation to $\Phi(t)$ was obtained by using, on the elements adjacent to $\frac{3}{2}\pi$ reentrant corners, suitably defined basis functions with this limiting behavior. Because the continuity condition on Φ' cannot be imposed at a reentrant corner, an alternative linear equation was required. This was obtained by use of Eq. (15) through order $|s-s_c|^2$ to relate values of Φ_j for $j=l_c$ and $l_c \pm 1$ and values of Φ'_j for $j=l_c \pm 1$. (The approximations to Φ on the singular elements adjacent to corner nodes do not involve the parameter Φ'_{l_c} , which was left undefined for singular elements.)

B. Shapes investigated

Numerical calculations were carried out for many variations of the geometry shown in Fig. 1. Five series of calculations were carried out for viscometers with the duct ends flush with the chamber walls ($L_i=0$). For each series the duct radius was varied from $0.02 r_c$ to $0.5 r_c$. The series differ in the ratio of the lengths r_c , L_c , and L_d . For series C these lengths were in the ratio 1:2:2. The effects of halving and doubling the duct length were checked with series B (1:2:1) and D (1:2:4). The effects of halving and doubling the chamber lengths were checked with series A (1:1:2) and E (1:4:2). The duct-end effects were found to depend most strongly on the ratio r_d/r_c and only weakly on the other dimensions. The effects of rounding the orifice edges were investigated mainly with the series C shapes, but checked with series A.

For the viscometers with $L_i \neq 0$, as used in recent experiments, the duct extends into the chambers a distance L_i (the insertion length). The dependence of the orifice parameters on this length was investigated for a shape typical of the shapes used in recent experiments.² The effects of duct-wall thickness were also calculated.

C. Grid generation

Uniform spacing of the nodes does not yield optimum approximations of the eigenfunctions. Instead, the node spacings h_j were scaled to provide greater detail in regions where the eigenfunction was varying most rapidly, i.e., near reentrant corners. The numerical code was constructed so that a maximum node spacing h_{\max} was used for surfaces where Φ is weakly varying. The spacing was uniformly graded down to a minimum node spacing h_{\min} at reentrant corners, as shown in Fig. 3. The figure shows two singular elements of length h_{\min} at the sharp corner, with neighboring normal elements of the same length, next-nearest neighboring elements graded up one step, etc. Various grading scales were tested. Typically the ratio of the lengths of adjacent elements was chosen to be between 1.05 and 1.1. The maximum and minimum node spacings were typically $h_{\max} = r_c/40$ and

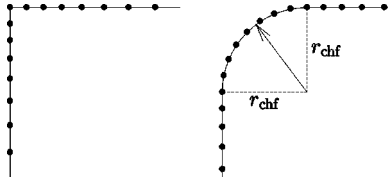


FIG. 3. Node positions near sharp and chamfered corners.

$h_{\min} = r_c/4000$ or $r_c/400$. The number of elements N varied from 216 to 404, depending on the series and on h_{\min} . The results reported in this paper have been calculated with many grid configurations and do not depend significantly on the details of the grids used.

The effects of chamfering reentrant corners was investigated by replacing the singular elements and adjacent straight elements by circular-arc elements; the node spacing on the circular-arc elements was always h_{\min} , with h_j graded upward in the straight elements adjacent to the circular-arc elements.

IV. NUMERICAL RESULTS

Figure 4 shows the cross-section of a viscometer and the numerically computed values of Φ_j and $|\Phi'_j|$. As expected, the eigenfunction is nearly constant within the chamber, and has a nearly linear dependence within the duct. The behavior near the duct orifice is more visible in the plot of $|\Phi'_j|$, which clearly shows the singular behavior. The singular behavior near the orifice edge is shown more clearly in Fig. 5. (The use of nonsingular basis functions in the elements adjacent to the reentrant corner yielded numerical values of Φ_j and Φ'_j nearly identical to those plotted here.)

Equation (10), with $\Omega(r') = 4\pi$ at internal points r' , can be used to calculate internal values of the velocity potential from the boundary values. Figure 2 shows some typical results near an orifice of a duct extending into a chamber. The

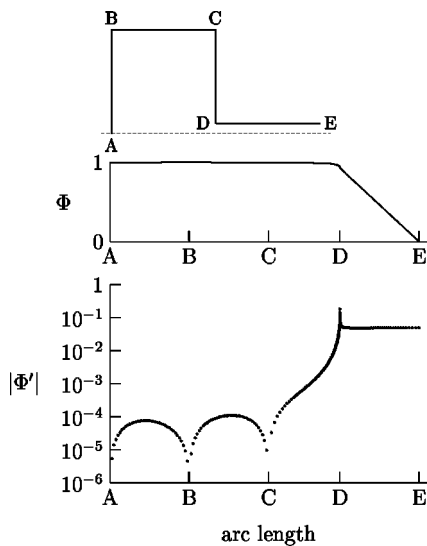


FIG. 4. Top: Outline of viscometer cross-section, with $L_c = r_c = L_d/2$ and $r_d = r_c/10$. Center and bottom: plots of Φ_j and $|\Phi'_j|$ at 321 nodes along the viscometer boundary, as a function of arc length along the boundary from reference point A to reference point E. The computed eigenvalue for this case is $k = 0.00245150/r_d$.

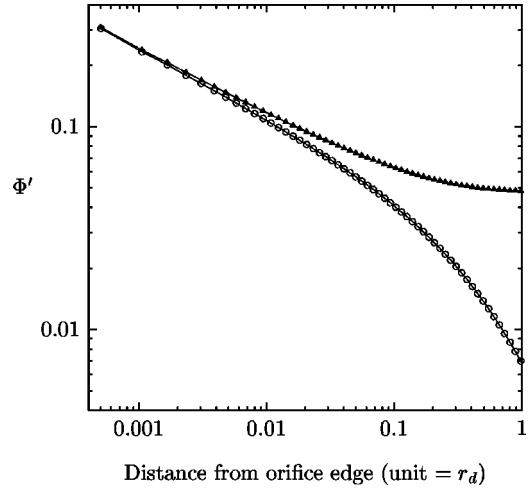


FIG. 5. The tangential derivative Φ' at nodes in the duct (triangles) and chamber (open circles) near the orifice, as functions of the distance from the orifice edge in units of the duct radius r_d , showing the expected divergent behavior. Viscometer dimensions are $r_c = L_c = L_d/2$, $r_d = r_c/10$.

flow pattern is typical; within the chamber the acoustic velocity drops rapidly over a distance of order r_d .

A. Eigenvalues and inertial end corrections

For each shape investigated, the eigenvalue k was calculated with at least two grid configurations. The results typically agreed to within a few parts in 10^8 . A convenient method of summarizing the results is to use the numerical value of k and the viscometer dimensions, together with the equivalent-circuit model in the limit of no dissipation, and to calculate the inertial end correction δ_j . Somewhat greater consistency of the results can be obtained by the separation $\delta_j = \delta'_j + \delta''_j$, where most of the effects of chamber length are included in the term δ''_j .

In Appendix A it is shown that a cylindrical chamber with a concentric circular orifice in which the normal fluid velocity is $u_z(r)$ has an input impedance equal to the sum of

$$Z'_{\text{in}} = \frac{\rho c^2}{i\omega V} \frac{kL_c}{\tan kL_c} \quad (17)$$

and

$$Z''_{\text{in}} = \frac{4ik\rho c}{\pi r_d} \sum_{n=1}^{\infty} \frac{A_n J_1(z_{0n} r_d / r_c)}{[z_{0n} J_0(z_{0n})]^2} F_n(k). \quad (18)$$

Here z_{0n} is the n th root of $dJ_0(z)/dz = 0$. The other quantities are

$$A_n = \int_0^{r_d} \tilde{u}_z(r) J_0(z_{0n} r / r_c) r dr, \quad (19)$$

where $\tilde{u}_z(r)$ is $u_z(r)$ divided by its value averaged over the orifice, and

$$F_n(k) = \frac{\coth[(z_{0n} L_c / r_c) \sqrt{1 - (kr_c / z_{0n})^2}]}{\sqrt{1 - (kr_c / z_{0n})^2}} \approx 1. \quad (20)$$

The first contribution, Eq. (17), is the zero-dissipation input impedance of the chamber modified for its finite length through the factor

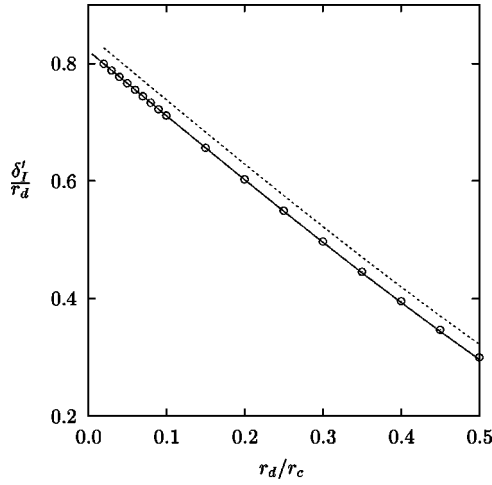


FIG. 6. Inertial end corrections δ'_l calculated from numerical eigenvalue k . The solid line was calculated for a model flow field in the orifice. The dotted line is Ingard's result for uniform flow in the orifice.

$$kL_c / \tan(kL_c) = 1 - \frac{1}{3}(kL_c)^2 + O(kL_c)^4. \quad (21)$$

Equation (17) is thus approximately

$$\mathbf{Z}'_{in} \approx \frac{\rho c^2}{i\omega V} + \frac{i\omega\rho L_c}{3\pi r_c^2}. \quad (22)$$

The second term has the frequency/phase signature of an inertial term; the corresponding contribution to δ_l is

$$\delta'_l = \frac{1}{3}(r_d/r_c)^2 L_c. \quad (23)$$

Similarly, the larger contribution to δ_l from Eq. (18) is

$$\delta'_l = 4r_d \sum_{n=1}^{\infty} \frac{A_n J_1(z_{0n} r_d / r_c)}{[z_{0n} J_0(z_{0n})]^2} F_n(k). \quad (24)$$

The inertial end corrections δ'_l were calculated for each resonator geometry using the numerical values of k and a modified form of Eq. (8), in which V_c was replaced by $V_c \tan(kL_c)/(kL_c)$, so that the effects of finite chamber size expressed in Eq. (17) are accounted for. Average results for the five series of viscometers are shown in Fig. 6. The results for the individual series differ from the average by a maximum of 0.001 at $r_d/r_c = 0.5$, and by a much smaller amount in range of typical applications $r_d/r_c \leq 0.1$. Thus separation of the δ'' term accounts for nearly all dependence on viscometer dimensions other than the ratio r_d/r_c . A linear fit to the data in the range $r_d/r_c \leq 0.1$ yielded

$$\delta'_l / r_d = 0.82159 - 1.1020 r_d / r_c. \quad (25)$$

The correctness of this result is supported by the agreement, to five decimal places, of the constant term with the recent calculation of Norris and Sheng.²⁴

The decrease with increasing duct radius is due to the change in coupling to the chamber modes in Eq. (24). Ingard¹⁶ used a similar expression with a piston (constant) approximation to u_z in the orifice, for which

$$A_n = 2J_1(z_{0n} r_d / r_c) / (z_{0n} r_d / r_c).$$

The dotted line in Fig. 6 was calculated using this expression. It clearly overestimates the end correction. A better

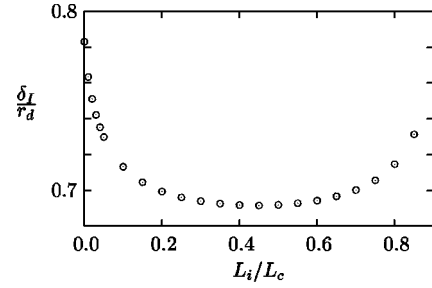


FIG. 7. Inertial end correction as a function of insertion length L_i , for a viscometer with $L_c = r_c = L_d/2$, $r_d/r_c = 0.05$, and $r'_d/r_c = 0.075$.

result is obtained by using an approximation to the actual flow

$$\tilde{u}_z = A + BX + CX^{-1/3}, \quad (26)$$

with $X = 1 - (r/r_d)^2$. The coefficients in this expression were obtained by calculating internal values of Φ for a series A viscometer with $r_d/r_c = 0.05$. The results (similar to those in Fig. 2) were numerically differentiated to obtain u_z in the plane of the orifice. Equation (26) was fit to the results to obtain the coefficients $A = 0.249 \pm 0.002$, $B = 0.032 \pm 0.002$, and $C = 0.490 \pm 0.001$. With these coefficients, the A_n were computed using Eqs. (19) and (26), and $\delta'_l/r_d = 0.7666$ was obtained by summing Eq. (24), in excellent agreement with the value 0.7665 obtained from the numerical eigenvalue and the model. Under the assumption that Eq. (26) with these coefficients is a reasonable approximation to \tilde{u}_z for the other values of r_d , Eq. (24) was then used to calculate δ'_l/r_d as a function of r_d/r_c . The results, shown as the solid line in Fig. 6, show that this approximation gives an excellent account of the orifice inductance.

The inertial end correction has also been calculated for viscometers with a finite insertion length $L_i > 0$. Unfortunately the insertion of the duct end distorts the resonator shape so that the contribution δ'_l can no longer be calculated in a simple way. Instead, the full inertial end correction must be calculated for each resonator geometry, using the numerical eigenvalues and an equivalent circuit with the input impedances of the chambers equal to $\rho c^2 / i\omega V_c$. Results as a function of L_i/L_c are shown in Fig. 7 for a typical viscometer. The inertial end correction decreases initially as L_i increases from zero, reaches a minimum, and then increases again as the interaction with the back wall of the chamber increases. When the duct end is near the center of the resonator it most closely approximates an un baffled end, with maximum distance to the chamber walls. The minimum value exceeds the value of Levine and Schwinger⁹ for an un baffled duct of zero thickness because the finite thickness of the duct acts as a partial baffle. The dependence on duct thickness is shown in Fig. 8. For each value of the fractional duct thickness $(r'_d - r_d)/r_d$, the end correction δ_l was found to be a linear function of r_d/r_c , and consistent with the trend in Fig. 6. The data were extrapolated to zero duct thickness to obtain the top curve in Fig. 8, which appears to smoothly approach the Levine–Schwinger value of 0.61 for zero fractional duct thickness.

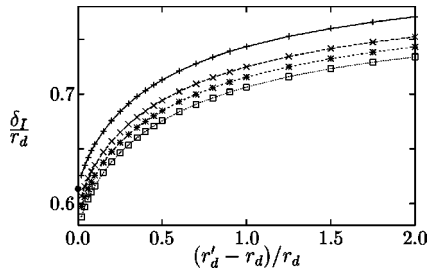


FIG. 8. Inertial end correction as a function of fractional duct thickness $(r'_d - r_d)/r_d$, for r_d/r_c equal to 0.1, \square , 0.075, $*$, 0.05, \times , and extrapolated to zero, $+$. The single solid circle \bullet represents the result of Levine and Schwinger in the limit of zero duct thickness. The other resonator dimensions were $L_c = 2r_c$, $L_d = 5r_c/2$, and $L_i = r_c/2$.

B. Acoustic flow in the duct

The resonance frequencies of Greenspan viscometers are typically much lower than the cutoff frequencies for higher modes of a duct. Accordingly, near the center of the duct, the eigenvector is expected to be well approximated by a multiple of $\sin kz$, and the tangential derivative by a multiple of $\cos kz$. Insight into the divergent flow near the orifice can be gained by looking at the difference between Φ' in the duct and the best approximation $A \cos kz$. This difference $\Delta\Phi' = \Phi' - A \cos kz$ is plotted in Fig. 9. The constant A was determined by a fit to Φ' for $z < L_d/4$. The figure shows that the difference is smooth over five orders of magnitude. The divergent behavior of the tangential derivative near the orifice is evident. The complete solution in the duct can be expressed as the sum of the propagating mode and an infinite number of evanescent modes, the latter approximately proportional to $\exp(-z_{0n}\Delta z/r_d)$, where Δz is the distance from the orifice edge. The line in Fig. 9, which is proportional to the $n=1$ evanescent wave, is clearly a good approximation to the plotted data in an intermediate range away from the

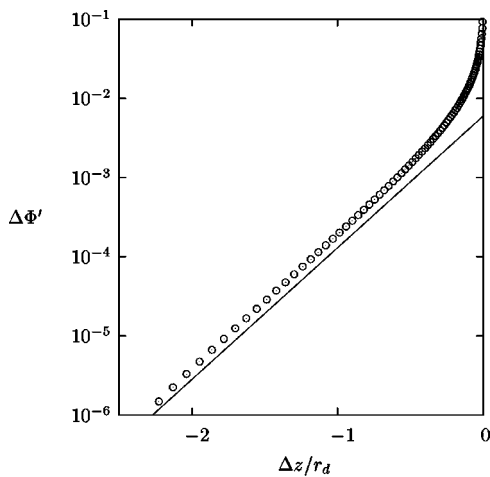


FIG. 9. Difference $\Delta\Phi' = \Phi' - A \cos kz$ between the tangential derivative of the velocity potential in the duct and $A \cos kz$, plotted as a function of the distance Δz from the orifice edge, for a viscometer with $L_c = r_c = L_d/2$ and $r_d/r_c = 0.1$. The constant A was determined by a fit to Φ' well within the duct. The differences near the orifice can be expressed in terms of an infinite sum of evanescent waves. The decay constant for the most-slowly decaying evanescent wave is shown as a solid line.

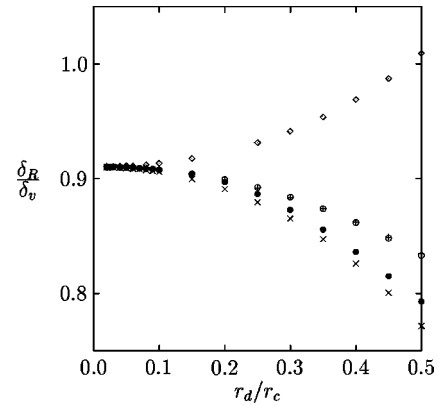


FIG. 10. Orifice resistance parameter as a function of duct radius, for five Greenspan viscometers with $L_1 = 0$; Series A, \times ; B, \bullet ; C, \circ ; D, $+$; E, \diamond .

orifice but above the digital noise farther into the duct. This agreement provides further support for the correctness of the numerical calculations.

C. Orifice resistance

For each set of numerical calculations, the ratio δ_R/δ_v was calculated using Eqs. (5)–(7). The integral for P was calculated from the cubic representation of Φ' on each element and the numerically determined values of Φ_j and Φ'_j . The results are shown in Fig. 10 for the five series of resonators with duct ends flush with the chamber wall. For small duct radii, the orifice resistance parameter approaches 0.909 ± 0.001 for all series. The contribution from outside the duct approaches 0.499, and the contribution from inside the duct approaches 0.410.

The orifice resistance parameter was calculated as a function of insertion length for one case. The results are shown in Fig. 11. As the duct insertion increases from zero, the orifice resistance begins increasing rapidly, reaches a plateau, and then rises further as the duct end nears the back wall of the chamber. The initial increase is a trend toward an unbauffed duct end. When the duct is flush with the chamber wall the local field approximates that near an infinite baffle, where there is a single integrable singularity in the square of the tangential velocity. When the duct extends into the chamber there is a second singularity of the same order at the outer corner of the duct end. The numerical coefficient of the outer singularity increases as the duct wall thickness decreases. When the duct gets very thin, the combination of singularities approximates the stronger singularity of an in-

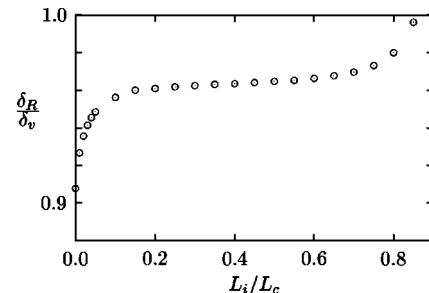


FIG. 11. Orifice resistance parameter as a function of insertion length L_i , for a viscometer with $L_c = r_c = L_d/2$, $r_d/r_c = 0.05$, and $r'_d/r_c = 0.075$.

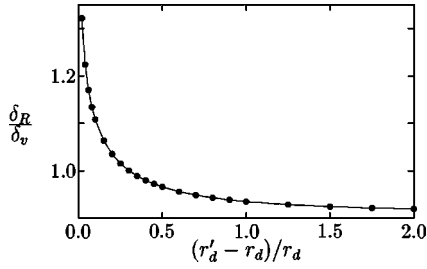


FIG. 12. Orifice resistance parameter as a function of relative duct thickness $(r'_d - r_d)/r_d$, for a resonator with $L_c = 2r_c$, $L_d = 5r_c/2$, and $L_i = r_c/2$. Calculations were made for r_d/r_c equal to 0.1, 0.075, and 0.05. The dependence of δ_R/δ_v on r_d/r_c was negligible.

finitesimally thin duct, so that the orifice resistance increases with decreasing duct thickness, as shown in Fig. 12.

D. Rounded corners

The effects of rounding sharp reentrant corners on the inertial and resistive end corrections have been investigated. The sharp orifice edge was replaced by a quarter-circular arc of radius r_{chf} . Orifice inertance and resistance parameters were calculated as a function of r_{chf} for a large variety of conditions. The resistive end corrections were found to scale according to

$$\delta_R(r_{\text{chf}}) = \delta_R(0) \left[1 - \frac{1}{3} (r_{\text{chf}}/r_d)^{1/3} \right]. \quad (27)$$

The inertial end correction was only weakly dependent on chamfering, as expressed by the scaling law

$$\delta_I(r_{\text{chf}}) = \delta_I(0) \left[1 - 30.3 (r_{\text{chf}}/r_c)^{4/3} \right]. \quad (28)$$

The occurrence of the chamber radius in the latter suggests that the effect is associated with the slope in Fig. 6 rather than the intercept.

The decreases of both δ_R and δ_I by rounding of the sharp corners is qualitatively consistent with the trend observed in Thurston's measurements of the effects of severe beveling and rounding on the impedance of orifices in thin plates.¹⁸ A more quantitative test was made during the development of the Greenspan viscometer.² The ends of a duct were chamfered slightly, so that $r_{\text{chf}}/r_d \approx 0.07$. The corresponding decrease in δ_R predicted by Eq. (27) is 14%, which was confirmed experimentally within about 4%. The predicted and observed changes in δ_I were less than 1%.

V. CONCLUDING REMARKS

The boundary-integral-equation formalism described here has been shown to be a useful technique for calculating the acoustic field within Greenspan viscometers, including the singular effects near reentrant corners. The resulting acoustic solutions were used together with a boundary-layer approximation for the vorticity mode to determine the inertial and resistive components of the lumped acoustic impedances associated with the duct ends. Limiting cases of the results were shown to agree with known results for baffled and unbaffled duct ends. The reduction of the acoustic resistance at duct ends was found to follow a power law. In future applications, the results can be applied to the design of duct

ends with rounded edges to minimize the maximum tangential velocity, a possible source of nonlinear effects.

ACKNOWLEDGMENTS

The author has had many helpful conversations with Michael Moldover and Keith Gillis. This work was supported in part by the Office of Naval Research.

APPENDIX A

An expression for the acoustic input impedance of a circular orifice in one end of a cylindrical chamber is derived in this section. The cylinder has rigid walls at $r=r_c$, $z=0$, and $z=L_c$. The orifice is at $z=0$, $r \leq r_d$. The normal component of the acoustic velocity in the plane of the orifice is $u_z(r)$. The acoustic pressure in the chamber can be expressed using Green's theorem

$$p(\mathbf{r}') = 2\pi i \omega \rho \int_0^{r_d} u_z(r) G(\mathbf{r}, \mathbf{r}') r dr. \quad (A1)$$

The Green's function is

$$G(\mathbf{r}, \mathbf{r}') = \sum_{nl} \frac{\epsilon_l \Phi_{nl}(r, z) \Phi_{nl}(r', z')}{\pi r_c^2 L_c [J_0(\zeta_{0n})]^2 (k_{nl}^2 - k^2)}, \quad (A2)$$

where $\epsilon_l = 2 - \delta_{l0}$ is the Neumann symbol, the eigenfunctions are

$$\Phi_{nl} = J_0(\zeta_{0n} r/r_c) \cos(l\pi z/L_c), \quad (A3)$$

the eigenvalues are

$$k_{nl}^2 = (\zeta_{0n}/r_c)^2 + (l\pi/L_c)^2, \quad (A4)$$

$J_m(\zeta)$ is a Bessel function, and ζ_{0n} the n th root of $J'_0(\zeta) = -J_1(\zeta) = 0$. The specific acoustic input impedance of the orifice is the ratio of the mean pressure in the orifice $\langle p \rangle$ to the volume velocity $\langle u_z \rangle A_d$. The mean pressure can be obtained by averaging

$$p(r, z) = \frac{2i\omega\rho\langle u_z \rangle r_d^2}{r_c^2 L_c} \sum_{nl} \frac{\epsilon_l A_n}{[J_0(\zeta_{0n})]^2} \times \frac{J_0(\zeta_{0n} r/r_c)}{(\zeta_{0n}/r_c)^2 + (l\pi/L_c)^2 - k^2}, \quad (A5)$$

where

$$A_n = \int_0^{r_d} \tilde{u}_z(r') J_0(\zeta_{0n} r'/r_c) r dr \quad (A6)$$

and \tilde{u}_z is $u_z/\langle u_z \rangle$. Note that $A_0 = \frac{1}{2}$, so that the $n=0$ sum can be split off. The input impedance of the chamber is

$$\mathbf{Z}_{\text{in}} = \frac{\langle p \rangle}{\rho c \langle u_z \rangle} = \frac{i\omega\rho}{A_d} \frac{r_d^2 L_c}{\pi^2 r_c^2} \mathcal{S}(ikL_c/\pi) + \frac{i\omega\rho}{A_d} \frac{4ir_d L_c}{\pi^2 r_c} \sum_{n=1}^{\infty} \frac{A_n J_1(\zeta_{0n} r_d/r_c)}{\zeta_{0n} [J_0(\zeta_{0n})]^2} \mathcal{S}(\alpha_n), \quad (A7)$$

where

$$\mathcal{S}(\alpha) = \sum_{l=0}^{\infty} \frac{\epsilon_l}{l^2 + \alpha^2} = (\pi/\alpha) \coth(\alpha\pi),$$

$$\alpha_n = \zeta_{0n} L_c \eta_n(\pi r_c) \eta_n,$$

$$\eta_n = \sqrt{1 - (kr_c/\zeta_{0n})^2} \approx 1.$$

The input impedance is the sum of two terms equivalent to Eqs. (17) and (18).

APPENDIX B

Consider the integral equation (10) for axisymmetric problems with source points $\mathbf{r}(t) = (r, z, \phi)$ and field points $\mathbf{r}(t') = (r', z', 0)$. The distance $R = |\mathbf{r}(t) - \mathbf{r}(t')|$ is

$$R(t', t, \phi) = \sqrt{r^2 + r'^2 - 2rr' \cos \phi + (z - z')^2}. \quad (\text{B1})$$

The area element is $dS = r d\phi h dt$, where

$$h(t) = ds/dt = \sqrt{(dr/dt)^2 + (dz/dt)^2}.$$

For solutions independent of ϕ , Eq. (10) can be integrated over ϕ to obtain Eq. (12), where the kernel is

$$g_n(t', t) = \mathbf{n}(t) \cdot \int_0^{2\pi} \nabla R \frac{d}{dR} \left(\frac{\exp(ikR)}{R} \right) d\phi. \quad (\text{B2})$$

The basis set for approximate solutions of Eq. (12) can be defined as follows. The parameter t is scaled so that the j th element corresponded to $j-1 \leq t \leq j$. The local coordinate on element j is $\tau_j = t - j + 1$. The functions $H_m^j(\tau_j)$ are defined to vanish for $\tau_j < 0$ and $\tau_j > 1$, and to equal $H_m(\tau_j)$ on element j , where

$$\begin{aligned} H_1(\tau) &= 1 - 3\tau^2 + 2\tau^3, & H_2(\tau) &= \tau(1 - \tau)^2, \\ H_3(\tau) &= 3\tau^2 - 2\tau^3, & H_4(\tau) &= -\tau^2(1 - \tau). \end{aligned} \quad (\text{B3})$$

The linear combination

$$\begin{aligned} \Psi(t) &= \sum_{j=1}^N [\Phi_{j-1} H_1^j(\tau_j) + h_j \Phi'_{j-1} H_2^j(\tau_j) + \Phi_j H_3^j(\tau_j) \\ &\quad + h_j \Phi'_j H_4^j(\tau_j)] \end{aligned} \quad (\text{B4})$$

interpolates Φ and its derivative Φ' with respect to arc length at all nodes. This form was used to approximate the solution $\Phi(t)$. For the linear and circular elements used in this work the derivative Ψ' is continuous at all nodes. As noted in the main text, a series expansion of Eq. (15) through order $|s - s_C|^2$ was used instead of Eq. (B4) on elements adjacent to a reentrant corner. The form of the expansion insured continuity of Ψ at the reentrant corners, but not of the derivatives. The form of the expansion was chosen to match Φ and Φ' at the adjacent nodes.

A numerical approximation to the integral equation (12) was obtained by using Eq. (B4) to approximate Φ , and requiring that the approximate form hold at the $N+1$ nodes t'_i . This yielded a set of $N+1$ linear equations of the form

$$-\Omega_i \Phi_i = \sum_{j=0}^N [B_{ij} \Phi_j + C_{ij} \Phi'_j], \quad (\text{B5})$$

with suitably defined B_{ij} and C_{ij} determined by integrations of the kernel over the elements. Continuity of Ψ'' at all non-reentrant internal nodes requires

$$\begin{aligned} 6(\Phi_{j-1} - \Phi_j)/h_j^2 + 2(\Phi'_{j-1} + 2\Phi'_j)/h_j \\ = -6(\Phi_j - \Phi_{j+1})/h_{j+1}^2 - 2(2\Phi'_j + \Phi'_{j+1})/h_{j+1}. \end{aligned} \quad (\text{B6})$$

An alternative condition for reentrant corners was obtained by using the values of Ψ'' from the series expansion of Ψ on the singular elements, and matching these to values on the adjacent nodes. As explained in the main text, these equations were supplemented by conditions on the first and last elements to permit a solution in the form of Eq. (13), which was then used to eliminate the derivatives from Eq. (B5) to obtain Eq. (14).

The matrix elements were calculated using the Quadpack adaptive numerical quadrature routine `qndaa`.²⁸ Special care was taken with the weakly singular integrals which occurred when the range of integration included the collocation point t'_j . The singularities were of the logarithmic form, and were handled using identities similar to

$$\int_0^1 f(t) \log t dt = -f(0) + \int_0^1 [f(t) - f(0)] \log t dt.$$

This procedure separated out the singular contribution and permitted the use of a non-singular quadrature routine for the remaining integration. The error limits for the adaptive quadrature were set as low as feasible for IEEE double precision computations. No effort was made to optimize the speed of calculation by relaxing the error limits. Sufficient checks were made to insure that the accuracy of the quadrature did not influence the accuracy of the results.

- ¹K. A. Gillis, J. B. Mehl, and M. R. Moldover, "Greenspan acoustic viscometer for gases," *Rev. Sci. Instrum.* **67**, 1850–1857 (1996).
- ²K. A. Gillis, J. B. Mehl, and M. R. Moldover, in preparation.
- ³G. Kirchhoff, "Über den Einfluss der Wärmeleitung in einem Gase auf die Schallbewegung," *Ann. Physik Chem. (Fifth Ser.)* **134**, 177–193 (1868); English translation ("On the influence of heat conduction in a gas on sound propagation") by R. B. Lindsay in *Benchmark Papers in Acoustics: Physical Acoustics*, edited by R. B. Lindsay (Dowden, Hutchinson, & Ross, Stroudsburg, PA, 1974), pp. 7–19.
- ⁴Martin Greenspan and Francis N. Wimenitz, "An Acoustic Viscometer for Gases—I," NBS Report 2658 (1953).
- ⁵Lord Rayleigh, *The Theory of Sound*, 2nd ed. (Dover, New York, 1945), Vol. 2, Sec. 307, Appendix A.
- ⁶P. J. Daniell, "The coefficient of end-correction," *Philos. Mag.* **30**, 137–146 (1915); 248–256 (1915).
- ⁷L. J. Sivian, "Acoustic impedance of small orifices," *J. Acoust. Soc. Am.* **7**, 94–101 (1935).
- ⁸R. H. Bolt, S. Labate, and U. Ingard, "The acoustic reactance of small circular orifices," *J. Acoust. Soc. Am.* **21**, 94–97 (1948).
- ⁹H. Levine and J. Schwinger, "On the radiation of sound from an unflanged circular pipe," *Phys. Rev.* **73**, 383–406 (1948).
- ¹⁰A. K. Nielsen, "Acoustic resonators of circular cross-section and with axial symmetry," *Trans. Danish Acad. Tech. Sci.* **10**, (1949).
- ¹¹G. B. Thurston, "Periodic fluid flow through circular tubes," *J. Acoust. Soc. Am.* **24**, 653–656 (1952).
- ¹²G. B. Thurston and C. E. Martin, "Periodic flow through circular orifices," *J. Acoust. Soc. Am.* **25**, 26–31 (1953).
- ¹³A. W. Nolle, "Small-signal impedance of short tubes," *J. Acoust. Soc. Am.* **25**, 32–39 (1953).
- ¹⁴A. F. Kuckes and U. Ingard, "A note on acoustic boundary dissipation due to viscosity," *J. Acoust. Soc. Am.* **25**, 798–799 (1953).
- ¹⁵G. B. Thurston and J. K. Wood, "End corrections for a concentric circular orifice in a circular tube," *J. Acoust. Soc. Am.* **25**, 861–863 (1953).

- ¹⁶K. Ingard, "On the theory and design of acoustic resonators," J. Acoust. Soc. Am. **25**, 1037–1061 (1953).
- ¹⁷G. B. Thurston, L. E. Hargrove, and B. D. Cook, "Nonlinear properties of circular orifices," J. Acoust. Soc. Am. **29**, 992–1001 (1957).
- ¹⁸G. B. Thurston, "Nonlinear acoustic properties of orifices of varied shapes and edge conditions," J. Acoust. Soc. Am. **30**, 452–455 (1958).
- ¹⁹K. Ingard and H. Ising, "Acoustic nonlinearity of an orifice," J. Acoust. Soc. Am. **42**, 6–17 (1967).
- ²⁰Y. Ando, "On the sound radiation from semi-infinite circular pipe of certain wall thickness," Acustica **19**, 219–225 (1969/70).
- ²¹D. K. Holger, T. A. Wilson, and G. S. Beavers, "The inertance of a smooth-edged orifice," J. Acoust. Soc. Am. **51**, 1156–1163 (1972).
- ²²R. L. Panton and A. L. Goldman, "Correlation of nonlinear orifice impedance," J. Acoust. Soc. Am. **60**, 1390–1396 (1976).
- ²³M. R. Stinson and E. A. G. Shaw, "Acoustic impedance of small, circular orifices in thin plates," J. Acoust. Soc. Am. **77**, 2039–2042 (1985).
- ²⁴A. N. Norris and I. C. Sheng, "Acoustic radiation from a circular pipe with an infinite flange," J. Sound Vib. **135**, 85–93 (1989).
- ²⁵M. Bernard and B. Denardo, "Re-computation of Ando's approximation of the end correction for a radiating semi-infinite circular pipe," Acustica **82**, 670–671 (1996).
- ²⁶P. M. Morse and K. U. Ingard, *Theoretical Acoustics* (McGraw-Hill, New York, 1968), pp. 480–490 and Chap. 9, Problem 12.
- ²⁷Germund Dahlquist and Åke Björk, *Numerical Methods* (Prentice-Hall, Englewood Cliffs, NJ, 1974), Sec. 5.8.1.
- ²⁸R. Piessens, E. de Doncker-Kapenga, C. Uberhuber, and D. Kahaner, *Quadpack: A Subroutine Package for Automatic Integration* (Springer, New York, 1983).